Mechanical Fatigue Resistance of Polydiketopyrrolo-Pyrrole-Dithienylthieno[3,2-b]thiophene-Based Flexible Field-Effect Transistors

Paweł Kubik, Witold Waliszewski, Andrzej Nosal, Mariusz Tomczyk, Adrian Adamski, Maciej Gazicki-Lipman, Paul W. M. Blom, Tomasz Marszalek,* and Wojciech Pisula*

Mechanical durability is one of the main obstacles of flexible organic electronic devices. In this work, the fatigue behavior of flexible field-effect transistors based on a diketopyrrolo-pyrrole-dithienylthieno[3,2-b]thiophene polymer is reported. An especially for that purpose designed bending setup allows to perform precise multiple deformation cycles of the transistor channel area while monitoring the device behavior. The transistors show high operational stability upon 100 bending cycles at a radius of 500 µm. Bending at smaller radius of 100 µm leaves the functionality of the parylene dielectric intact but induces serious mechanical fractures in the semiconducting film. Despite macroscopic defects, the transistors still reveal good reliability including high charge carrier mobility, due to presence of sufficient pathways for the charge carrier transport and to a low gate leakage. It is also observed that thinner polymer films are more sensitive to the deformation-induced defects leading to a larger decrease in device performance, especially during the initial bending cycles. In thicker DPP-DTT films, the crack propagation less affects the semiconductor/dielectric interface, at which the main charge carrier transport take place, resulting in a more stable device operation. Therefore, the work provides fundamental understanding of the fatigue behavior of flexible transistors based on semiconducting polymers.

1. Introduction

Working as electrical switches, field-effect transistors (FETs) constitute basic elements of logic circuits. Mechanically flexible transistors play an important role in the realization of next-generation electronics but they require elastic and fatigue resistant components to ensure long lifetime of the devices working under conditions of mechanical stress. In contrast to rigid inorganic semiconductors, π-conjugated polymers are promising active materials for flexible electronics due to their low Young modulus and high elongation at yield.[1–3] As an additional advantage, polymer semiconductors show sufficiently high charge carrier mobility for many basic electronic applications. Furthermore, when substituted by alkyl side chains, π-conjugated polymers are soluble in most common organic solvents thus facilitating thin film deposition by solution processing[4,5] on lightweight and flexible substrates such as paper[6] or plastic foils.[4,7,8] The ease of processing together with their suitable mechanical properties open new perspectives for integration of π-conjugated polymers as semiconductors in rollable displays, sensors, or electronic skin.[3,9–12] However, the charge carrier transport as well as mechanical properties of conjugated polymer films strongly depend on their morphology and crystallinity.[13,14] High film crystallinity ensures unhindered charge carrier transport.[13] On the other hand, amorphous polymers are more resistant to mechanical stress than semicrystalline

P. Kubik, W. Waliszewski, A. Adamski, T. Marszalek, W. Pisula
Department of Molecular Physics
Faculty of Chemistry
Lodz University of Technology
Zeromskiego 116, Lodz 90-924, Poland
E-mail: marszalek@mpip-mainz.mpg.de; pisula@mpip-mainz.mpg.de

A. Nosal, M. Gazicki-Lipman
Institute of Materials Science and Engineering
Faculty of Mechanical Engineering
Lodz University of Technology
Stefanowskiego 1/15, Lodz 90-924, Poland

M. Tomczyk
Institute of Electrical Engineering Systems
Faculty of Electrical Engineering
Electronics, Computer and Control Engineering
Lodz University of Technology
Stefanowskiego 18, Lodz 90-924, Poland

A. Adamski
Department of Experimental Physics
Faculty of Fundamental Problems of Technology
Wroclaw University of Science and Technology
Wybrzeze Wyspianskiego 27, Wroclaw 50-370, Poland

P. W. M. Blom, T. Marszalek, W. Pisula
Max Planck Institute for Polymer Research
Ackermannweg 10, 55128 Mainz, Germany

**ADVANCED
SCIENCE NEWS**
www.advancedsciencenews.com

**ADVANCED
MATERIALS
INTERFACES**
www.advmatinterfaces.de

ones.[15–17] For example, disordered poly(3-hexylthiophene) (P3HT) films sustain much higher strain, without developing macroscopic cracks, than crystalline ones consisting of highly ordered nanofibrils. High crystallinity weakens mechanical flexibility of P3HT films and induces cracks at much lower strain.[18] In another example, organic field-effect transistors (OFETs) based on crystalline, molecular 6,13-bis(triisopropylsilylethynyl) pentacene (TIPS-pentacene) show higher increase of the electrical resistance during deformation due to the formation of mechanical defects compared to amorphous poly(triarylamine) (PTAA).[15] Mechanical properties of conjugated polymer films, including their tensile strength, yield point and elongation at yield, also improve with higher molecular weight.[1,14] Therefore, a trade-off between good charge carrier transport and mechanical properties is necessary for the application of conjugated polymers in flexible OFET devices.

In order to improve mechanical properties of conjugated polymers, modification of the backbone was carried out either by insertion of flexible spacers[19] or by control of the regional regularity of the polymers.[20] Such semiconducting copolymers may consist, for example, of flexible poly(ε-caprolactone) blocks alternating with diketopyrrolopyrrole (DPP) units.[21] In another concept, various side chains were attached to increase the elasticity of conjugated polymers including asymmetric and branched substituents.[22,23] Long aliphatic side chains attached to the polythiophene backbone lower the glass transition temperature and Young modulus. This leads to higher ductility and toughness as well as improves the ability of mechanical deformation without fracture.[24] Despite their amorphous nature, benzodithiophene-based polymers with a biaxially-extended side chain design also reveal high flexibility and a good charge carrier transport during deformation.[25] It was shown that polymers with abundant amorphous domains facilitate energy dissipation during stretching maintaining the charge carrier transport. The interdigitating and/or entanglement of these biaxially extended side chains are responsible for the mechanical robustness upon elongation.

The fatigue behavior of organic semiconducting films during cyclic deformation is a factor essential for practical applications. There are several reports related to that behavior, but most of them focus exclusively on mechanical properties of thin films.[1,26,27] The reports related to fatigue behavior of OFETs describe deformation of complete devices comprising the electrodes.[28–30] In this case, the bending stress spreads over the entire transistor architecture.

Most flexible applications require devices of low thickness to sustain serious deformation at small radii during rolling, wrinkling, or bending. Reduction of the device thickness leads to a decrease of the tensile strain at the top surface of the film during convex deformation. For this reason, a flexible substrate and dielectric layer are typically kept relatively thin to lower stresses at small bending radii of the transistor.[4,31,32] In order to evaluate electrical performance of flexible transistors in a controlled manner, multiple bending cycles on small radii are required to imitate realistic conditions during application. These studies are challenging due to handling thin devices, accurate deformation of the channel area at small radii and monitoring transistor response during bending. Most publications report device bending on a relatively large radius by simply wrapping the transistor around cylindrical or spherical objects.[33–35] Bending at smaller radii was performed by

folding,[9] wrinkling on prestretched elastomer[12,32,36] or placing the sample on a razor blade.[37] However, all these methods did not allow for a precise control of the deformation area and most of them were executed as a single bend of the device, thus not fully representing practical applications.

To better understand the fatigue behavior of semiconducting polymers in flexible OFETs, in this work, a setup for precise bending experiments was first designed and constructed. In that setup, the fatigued area and stress concentration are strictly confined to the transistor channel, which is a novel approach compared to literature. The setup permits bending cycles of flexile OFETs along the entire width of the transistor channel in such a way that the bending axis is oriented perpendicularly to the charge flow. The OFETs are deformed to small and well-defined radii of 100 and 500 µm, controlled by the curvature of a bending blade. After defined bending cycles representing different degree of fatigue load, OFET characteristics are recorded directly in the experimental setup. The OFETs in this work are based on poly[2,5-(2-octyldodecyl)-3,6-diketopyrrolopyrrole-alt-5,5-(2,5-di(thien-2-yl)thieno[3,2-b]thiophene)] (DPP-DTT, **Figure 1**a) as semiconducting donor-acceptor polymer and on Parylene C as gate dielectric layer and substrate. Poly(paraxylylene) derivatives (Parylenes) are known to be promising materials for substrate and dielectric layers in flexible transistors.[38] These polymers are deposited by chemical vapor deposition, which provides a fine control over the film thickness at large coverage areas.[39,40] The fatigue behavior was investigated for two different film thickness of DPP-DTT by monitoring the change in electrical performance as a function of bending cycles. The insight gained is fundamental for the development of flexible electronics with pronounced fatigue resistance and long application lifetime.

2. Results and Discussion

Mechanical strain induced on the surface of the OFET device during convex bending is inversely proportional to the bending radius (R) and is a function of the sample geometry as well as of the Young moduli of the materials involved. Tensile strain (ε) in the top layer during convex bending can be calculated using Equation 1:[41]

$$\varepsilon = \left(\frac{D_f + D_s}{2R} \right) \left(\frac{1 + 2\eta + X\eta 2}{(1 + \eta)(1 + X\eta)} \right) \tag{1}$$

where D_f denotes film thickness; D_s denotes substrate thickness; R denotes bending radius; and $\eta = D_f / D_s$; $X = E_f / E_s$ (where E_f and E_s are the Young moduli of the film and the substrate, respectively). In the case of $D_f \ll D_s$ ($\eta < 1$), this equation can be simplified to Equation 2:[41]

$$\varepsilon = \frac{D_f + D_s}{2R} \tag{2}$$

Tensile strain of the deformed DPP-DTT film was calculated using the simplified Equation 2, due to the low film thickness remaining between 30 and 120 nm, compared to the 4.5 µm
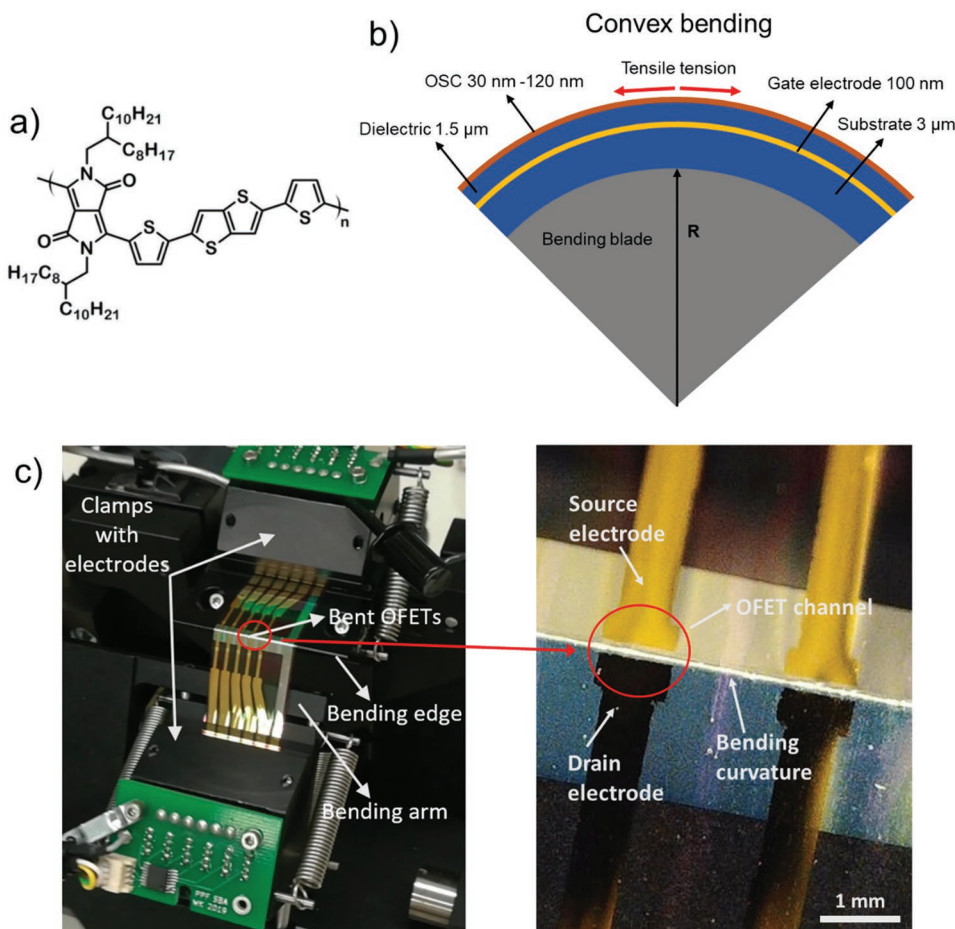
Figure 1. a) Chemical structure of DPP-DTT; b) schematic illustration of the channel area during convex bending; c) bending setup with flexible DPP-DTT-based OFETs bent over a blade at bending radius (*R*) of 100 μm (left image) and magnification of the 250 μm long transistor channel that is precisely placed over the bending blade (right image).

thick parylene substrate and dielectric. The OFETs were bent to the radii of 100 and 500 μm, thus inducing a calculated strain of 2.25% and 0.45%, respectively.

In order to investigate the fatigue behavior of the flexible OFETs during extensive cyclic bending, all device elements with their material properties have to be taken into account. Since the OFETs consist of a multilayer structure, comprising electrodes, dielectric and semiconductor layers, mechanical stability of the entire device depends on the mechanical properties of each single layer. Another important aspect are the stresses induced at the interfaces between the layers, especially when their Young moduli differ, potentially leading to delamination. These phenomena can seriously interrupt charge carrier injection and transport, which predominantly occur at the electrode/semiconductor and semiconductor/dielectric interfaces. As another consequence of defect formation, the electric field distribution can be distracted at the gate electrode/dielectric interface. Although this study focuses on the fatigue behavior of the active DPP-DTT film, mechanical resistance of the other device elements, that include the parylene dielectric, the gold electrodes and the interface between dielectric/gate electrode, was also taken into account, in order to confirm the robustness of the entire OFET architecture under the bending conditions applied.

As the first step, mechanical response of thermally evaporated 100 nm thick silver and gold electrodes towards cyclic deformation was investigated. As shown in Figure S1 (Supporting Information), conductivity of the electrodes remains unchanged after 1000 bending cycles for the radius of 100 μm, thus confirming their pronounced mechanical stability under these deformation conditions. Second, a potential delamination at the parylene dielectric/gate electrode interface was inspected by following electrical capacitance after deformation of a capacitor consisting of two silver electrodes evaporated on both sides of the parylene layer (Figure S2, Supporting Information). Since 100-fold bending of the capacitor at a radius of 100 μm does not change its capacitance (Table S1, Supporting Information), a delamination between the parylene dielectric film and the gate electrode can be excluded. The capacitance measurements did not also show any leakage current during the bending of the capacitor. This observation is in agreement with the very low gate leakage of OFETs after bending shown below in Figure 10. A delamination of the gold electrodes is also excluded because the bending axis is arranged between the contacts within the transistor channel as displayed in Figure 1c. As a conclusion of these initial studies, it is fair to state that the investigated device elements reveal high mechanical robustness under our

deformation conditions and consequently any changes of the OFET performance after bending can be solely attributed to the fatigue behavior of the DPP-DTT active film.

Before performing the bending cycles, the environmental stability of the DPP-DTT-based OFETs during exposure to ambient conditions for 6h was examined. These conditions correspond to the duration of the bending experiments in air. Additionally, the OFETs were stressed by tenfold on/off switching to prove operational device stability during the bending experiments. As shown in Figure S3 (Supporting Information), the OFET characteristics remain stable under these environmental and operational conditions. These results demonstrate that all further variations in OFET performance following deformation are only and exclusively related to the mechanical fatigue of the DPP-DTT film.

Both types of OFETs produced, i.e. those with 30 nm thick and those with 120 nm thick DPP-DTT layers, were exposed to 100 bending cycles at the radii of 100 and 500 μm. In order to gain information concerning structural changes taking place during the deformation, the OFET channel region of both types of devices was inspected with an optical microscope (OM). The OM images of films bent at a radius of 100 μm, presented in **Figure 2**a,b, reveal macroscopic wrinkles in the channel, which are aligned along the bending axis and thus perpendicular to the established stress. The wrinkles are attributed to an irreversible deformation formed beyond the elongation at yield of parylene. The 3D visualization presented in Figure 2c reveals a wrinkle height remaining between 1.0 and 2.5 μm and being independent of the DPP-DTT film thickness. In the case of OFETs bent to the radius of 500 μm, these defects do not occur since Parylene C does not undergo any irreversible deformation at strain of 0.45%.

The topography of the wrinkles in the DPP-DTT films (following 100 bending cycles at the radius of 100 μm) was investigated by means of atomic force microscopy (AFM). The AFM image of the 30 nm DPP-DTT film in **Figure 3**a displays cracks at the top of the wrinkles which are both arranged along the bending axis. The cracks are several micrometers long and, therefore, they are shorter than the channel width. Very likely, this still allows a formation of percolation pathways for the charge carrier transport between the defects. In the case of 30 nm thick film, the cracks are wider compared to the defects observed for the thickness of 120 nm (Figure 3b). No cracking was observed for OFETs bent to the radius of 500 μm (Figure S4, Supporting Information). This finding, resulting from the smaller strain of 0.45%, remains in a perfect agreement with the OM images.

The fractures observed in the bent DPP-DTT-based OFETs are considered a serious structural fatigue destruction potentially reducing the device performance. As described in literature, such macroscopic defects act as serious trapping sites limiting the charge carrier transport.[42] To study the impact of the ruptures induced in the DPP-DTT films on the device operation and to systematically evaluate the fatigue behavior of the flexible OFETs, the charge carrier transport was studied as a function of cycle number for the two film thicknesses of 30 and 120 nm and two bending radii of 100 and 500 μm. Before deformation, the 30 and 120 nm DPP-DTT-based OFETs reveal a good performance in ambient conditions with an average hole mobility of 0.35 cm^2 V^{-1} s^{-1}, on/off ratio close to 1×10^3 and threshold voltage (V_{th}) around −2 V, as derived from the device characteristics presented in **Figure 4**. After 5 bending cycles, the OFET performance remains quite stable as evident from the transistor parameters with an average charge
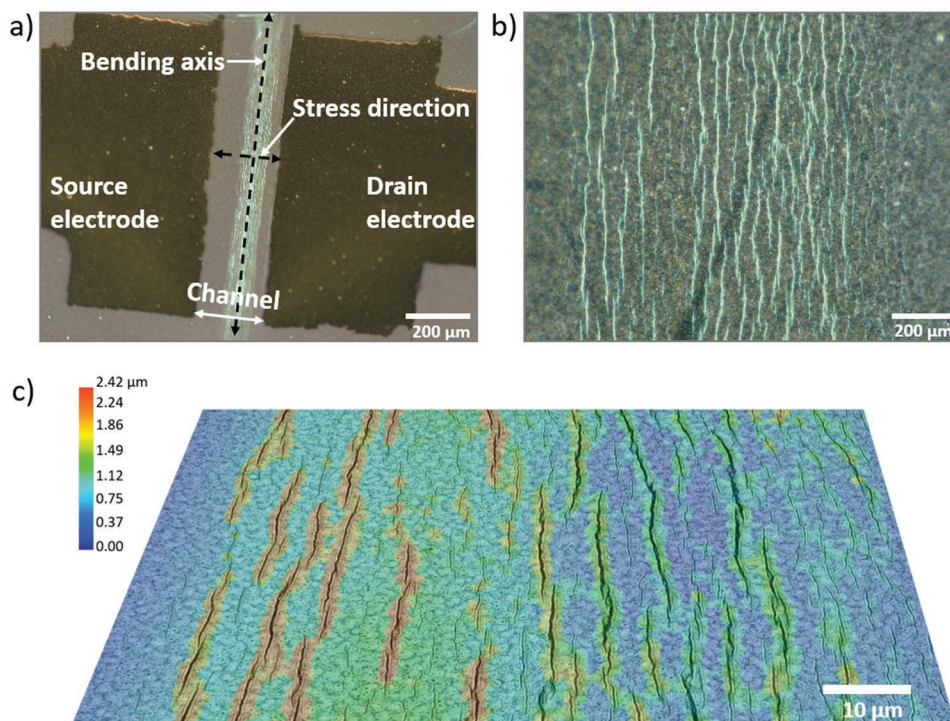
Figure 2. Optical microscopy images in (a) and (b) of wrinkles formed in the channel of a bent OFET at two different magnifications; c) 3D visualization of the wrinkles. The OFET is based on 30 nm DPP-DTT active film and was deformed 100 times to the radius of 100 μm.
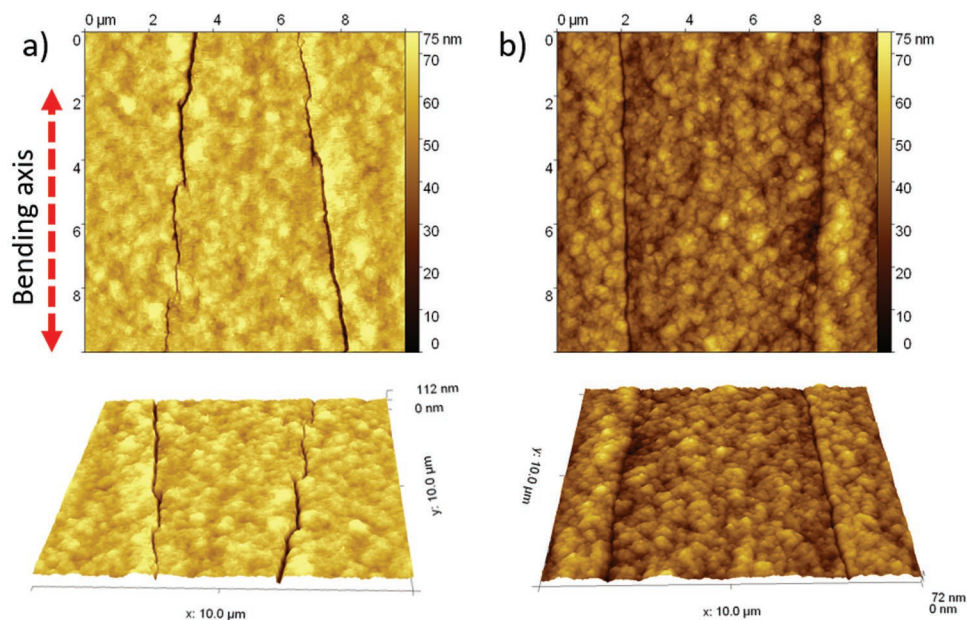
Figure 3. AFM height topography and 3D surface visualization of the DPP-DTT film in the channel region with thickness of a) 30 nm and b) 120 nm after 100 bending cycles at the radius of 100 μm.

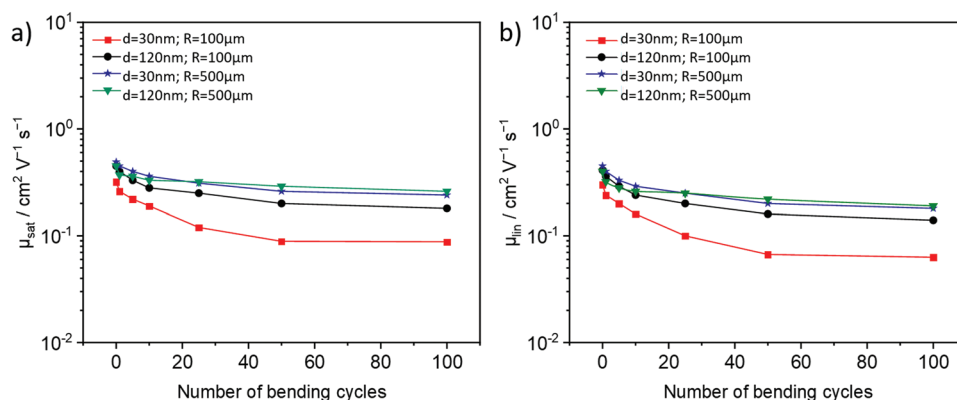carrier mobility of 0.24 cm² V⁻¹ s⁻¹, on/off of 8 × 10² and V_{th} of −5 V. It should be noted that in the transfer characteristics the slope of $\sqrt{I_{DS}}$ persists linear with only negligible hysteresis in the forward and backward sweeps, suggesting a close to ideal device behavior still after 5 bending cycles (Figure 4b). A slight decrease of the $I_{DS}(V_{GS})$ slope in the linear regime of the output characteristics, shown in Figure 4a, indicates certain increase in electrical resistance after deformation. To deeper understand the influence of the mechanical strain on the fatigue behavior of the DPP-DTT films, the OFET characteristics were recorded as a function of defined number of bending cycles and the corresponding charge carrier mobility is presented in **Figure 5**.

As evident from Figure 5, the charge carrier mobility of the 30 and 120 nm thick DPP-DTT films for both saturation and linear regimes is reduced only one quarter order of magnitude and remains therefore at nearly identical level during the bending cycles at the radius of 500 μm. The mobilities for the 120 nm film are 0.45 cm² V⁻¹ s⁻¹ before and 0.26 cm² V⁻¹ s⁻¹

after 100 cycles. This remains in a good agreement with the structural intactness of the DPP-DTT films observed by OM and AFM imaging. However, when the bending radius is reduced to 100 μm, the OFETs reveal stronger decline in charge carrier mobility. After 100 bending cycles, the values decrease from 0.32 to 0.088 cm² V⁻¹ s⁻¹ for the 30 nm thin film, and from 0.45 to 0.18 cm² V⁻¹ s⁻¹ for the 120 nm one. The main decline occurs during the initial 20 bending cycles, with the mobilities remaining constant for further cycles. These results reveal two trends related to the fatigue behavior of the flexible DPP-DTT OFETs. A higher film thickness of DPP-DTT and a large bending radius with lower stress induced result in a more stable carrier transport during cyclic deformation. Surprisingly, the decrease of the OFET performance bent at the radius of 100 μm is moderate taking into account severe macroscopic fractures in the semiconducting film. Especially in the case of the 120 nm thick film the difference in charge carrier mobility after 100 bending cycles is reduced by one third
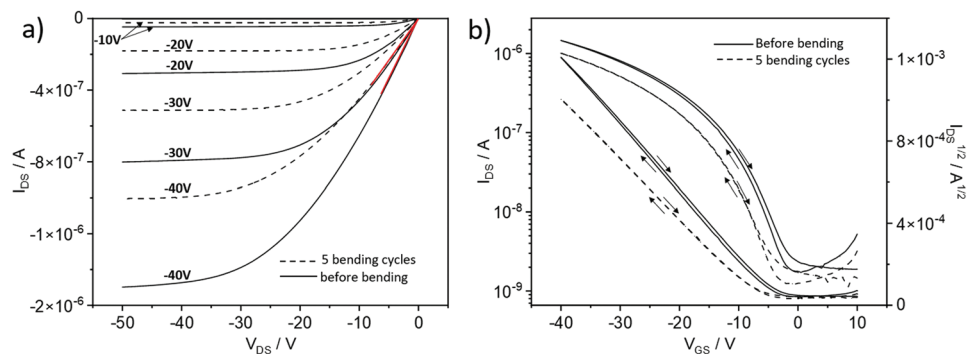
Figure 4. a) Output (red lines indicate I_{DS} slopes for $V_{GS} = −40$ V in the linear regime before and after 5 bending cycles) and b) transfer characteristics (recorded at V_{DS} −50 V) for the 30 nm DPP-DTT-based OFETs before and after 5 bending cycles at radius of 100 μm. Arrows indicate the sweep direction.

**ADVANCED
SCIENCE NEWS**

www.advancedsciencenews.com

**ADVANCED
MATERIALS
INTERFACES**

www.advmatinterfaces.de

Figure 5. a) Saturation and b) linear charge carrier mobility of flexible DPP-DTT-based OFETs as a function of the number of bending cycles for radii of 100 and 500 μm and film thicknesses of 30 and 120 nm.

order of magnitude. In addition, identical mobilities in the linear and saturation regimes, even after 100 bending cycles, indicate a pronounced homogenous order over the entire film thickness. A small decrease of the μ_{lin}/μ_{sat} ratio along with an increasing number of bending cycles implies a formation of certain defects in the active film upon deformation (Figure S5, Supporting Information). Interestingly enough, a quite high ratio is still recorded after 100 cycles and it is relatively independent of the film thickness and bending radius (Figure S5, Supporting Information). In order to gain understanding of
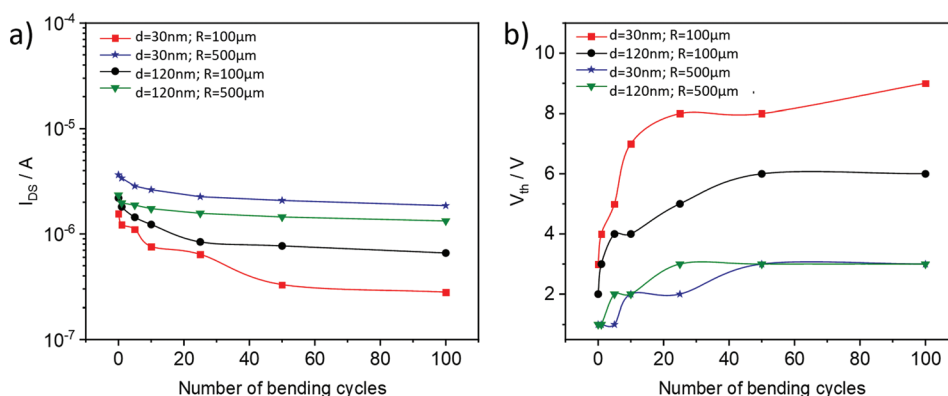
the relation between macroscopic defects induced by deformation and charge carrier mobility in DPP-DTT films of different thickness, the device characteristics are further analyzed.

The transfer characteristics of the OFETs, presented in **Figure 6**, reveal a consecutive decrease of I_{DS} at $V_{GS} = -40$ V with an increasing number of bending cycles, especially for the smaller bending radius of 100 μm. This is a result of the shift of the transfer curve to higher voltages, and also partly of a smaller slope of that curve. Thereby, the I_{DS} decrease depends on the film thickness and the bending radius. As seen in **Figure 7**a, for
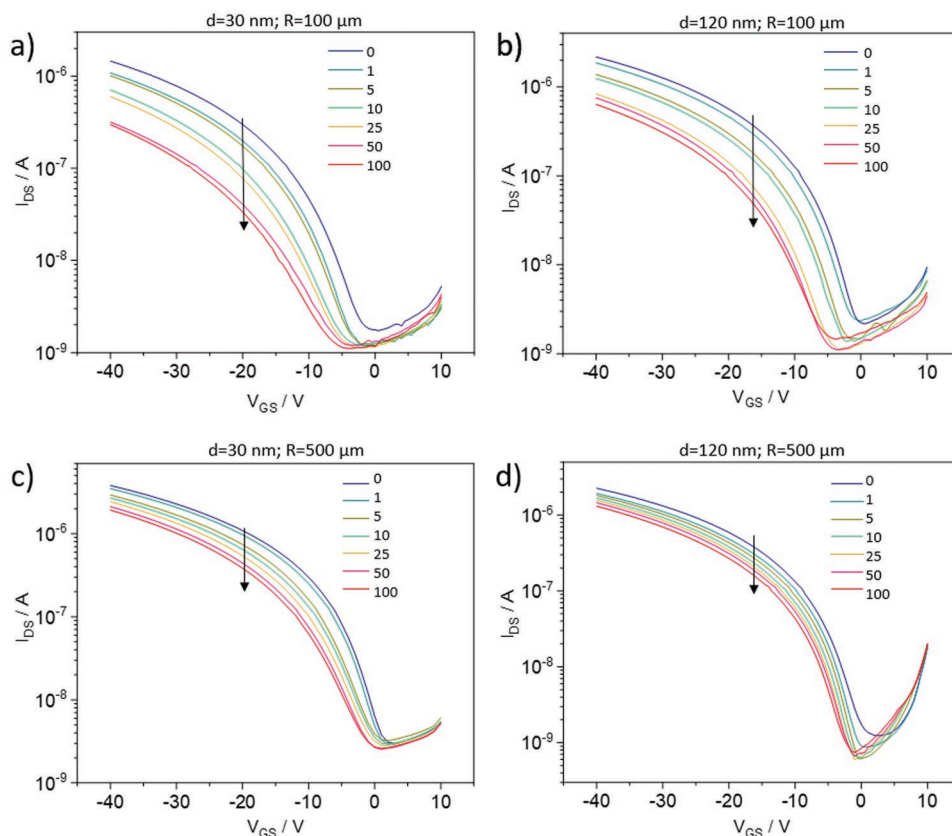
Figure 6. Transfer characteristics recorded at V_{DS} −50 V for flexible OFETs with 30 and 120 nm thick DPP-DTT films after multiple bending at the radius of a,b) 100 μm and c,d) 500 μm.

**ADVANCED
SCIENCE NEWS**

www.advancedsciencenews.com

**ADVANCED
MATERIALS
INTERFACES**

www.advmatinterfaces.de

Figure 7. a) I_{DS} at $V_{GS} = -40$ V and b) V_{th} of flexible OFETs based on 30 and 120 nm thick DPP-DTT as a function of bending cycles for radii of 100 and 500 µm.

both film thicknesses and for the bending radius of 500 µm, I_{DS} remains quite unchanged with increasing cycle number. Additionally, the shift of the transfer plots is marginal as expressed by the V_{th} increase from −1 to only −3 V, following 100 cycles (see Figure 7b). For the same reason, the charge carrier mobility is nearly constant during the fatigue deformation at the radius of 500 µm. Bending at the smaller radius of 100 µm induces a slightly larger shift of V_{th} from −3 to −9 V for the film thickness of 30 nm and from −2 to −6 V for that of 120 nm (Figure 7b). As a consequence, along with a partially smaller slope, I_{DS} decreases with an increasing cycle number leading to lower charge carrier mobilities. Among all the samples investigated, the strongest decline is observed in the case of the OFETs with 30 nm thick DPP-DTT layer, deformed at the radius of 100 µm. Similarly to the trend for the charge carrier mobility, the reduction of I_{DS} is most pronounced during the first 20 bending cycles, when it changes from 1.56×10^{-6} A to a constant value of 2.80×10^{-7} A. As a comparison, the same OFETs deformed at 500 µm show I_{DS} decline from 3.65×10^{-6} A to only 1.86×10^{-6} A. As mentioned before, the decrease in device performance for OFETs deformed at the radius of 100 µm is, nevertheless, surprisingly small regarding a presence of drastic fractures in the DPP-DTT films. The larger V_{th} shift to negative values with an increasing number of cycles indicates increased charge trapping at the OSC/gate dielectric interface or in the film bulk for the DPP-DTT films bent at the smaller radius.[43–46]

Reduced transistor performance after bending can be related to the effect of charge trapping in the mechanically fatigued DPP-DTT film. The trap density N_0 at the OSC/dielectric interface, calculated for different bending cycles,[47–50] is presented in **Figure 8** below. The calculation was based on the subthreshold slope (SS) of the transfer characteristics in the linear regime with the use of the following equation
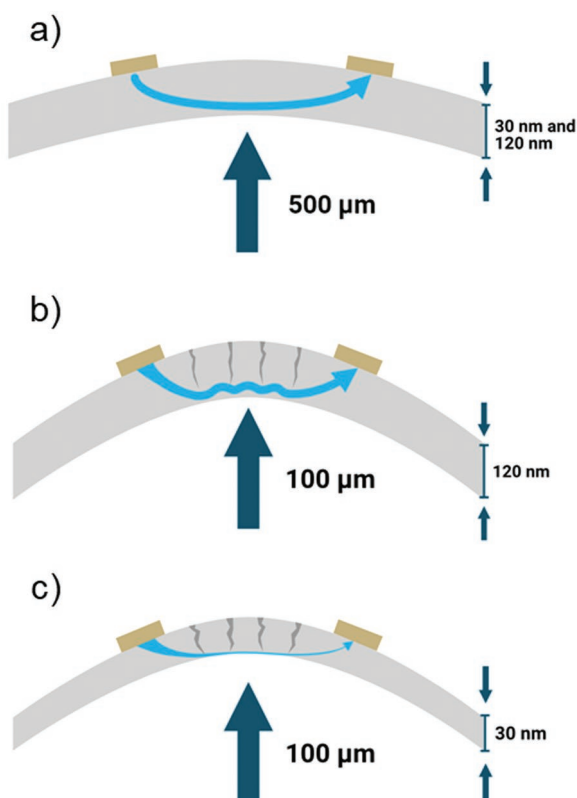
$$N_0 = \frac{Ci}{q}\left(\frac{SS \text{ x } \log e}{\frac{KT}{q}} - 1 \right) \qquad (3)$$

where N_0 denotes interface trap density; Ci denotes gate dielectric capacitance; K denotes Boltzmann constant, q denotes electronic charge; and T denotes absolute temperature.[47–50]

As seen in the figure, before deformation the 120 nm thick DPP-DTT films show lower N_0 of 4.5×10^{14} and 6.0×10^{14} cm² eV⁻¹ in comparison to the 30 nm thick layers exhibiting 7.5×10^{14} and 6.8×10^{14} cm² eV⁻¹ for the bending radii of 500 and 100 µm, respectively. The lower trap density of the thicker films well correlates with their higher charge carrier mobility which, in turn, is attributed to a smaller sensitivity of the parylene dielectric to the surface roughness ($R_a = 3$ nm). This might suggest that in the thicker layer the interfacial defects are by-passed more efficiently, while in the 30 nm thick film the by-passing is limited due to the reduced film thickness leading to more trapping.[51,52] With an increasing number of bending cycles at the radius of 500 µm, for both film thicknesses the trap density the DPP-DTT/dielectric interface slightly increases to 1.1×10^{15} cm² eV⁻¹ for 30 nm and to 9.1×10^{14} cm² eV⁻¹ for 120 nm. The small rise confirms the pronounced mechanical stability of the DPP-DTT films at the larger deformation radius (**Figure 9**a). Bending at the smaller radius of 100 µm more than doubles the trap density after 100 cycles for both film thicknesses. This implies that the DPP-DTT/dielectric interface is also mechanically affected upon deformation of the OFETs. It is assumed that the macroscopic cracks observed at the top surface of the DPP-DTT films penetrate the film leading to the interface defects such as trapping sites for the
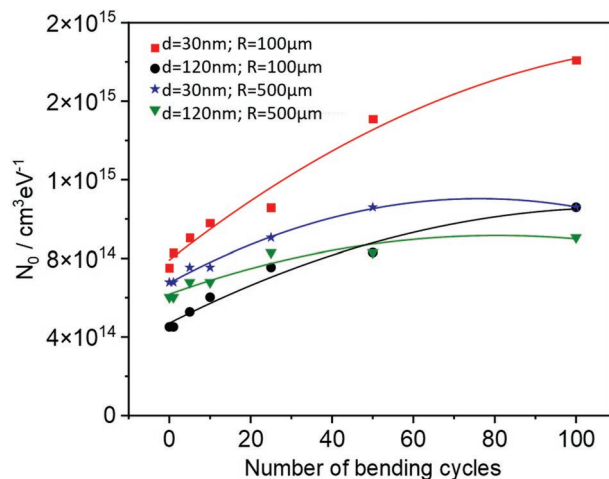

Figure 8. Trap density (N_0) of flexible OFETs based on 30 and 120 nm thick DPP-DTT as a function of bending cycles for radii of 100 and 500 µm.

2200206 (7 of 10)

**ADVANCED
SCIENCE NEWS**

www.advancedsciencenews.com

**ADVANCED
MATERIALS
INTERFACES**

www.advmatinterfaces.de

Figure 9. Schematic illustration of the fracture formation and charge carrier transport in the DPP-DTT film after multiple bending cycles of the flexible OFETs; a) after bending the OFETs at the radius of 500 μm, DPP-DTT films remain intact and the charge carrier transport is not disturbed; b) bending the 120 nm thick DPP-DTT film at smaller radius of 100 μm induces defects that do not reach the dielectric interface at which the transport takes place; c) the interface of the 30 nm thin film is more affected by the macroscopic fractures limiting the charge transport and reducing the OFET performance.

charges, as illustrated in Figure 9b,c. Smaller changes of the I_{DS} and V_{th} values for the 120 nm thick DPP-DTT film imply that the macroscopic fractures do not fully spread to the interface, while in the case of the thinner 30 nm film the defects in larger extent reach the interface and more strongly interrupt the charge carrier transport of the OFET.
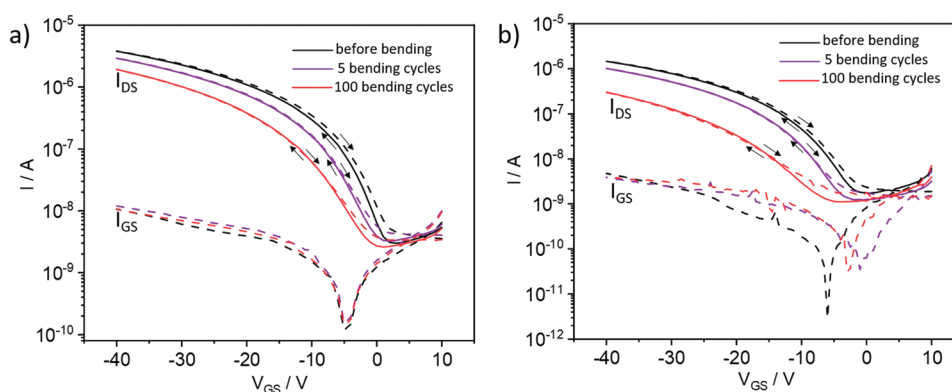
To determine the electronic robustness the parylene dielectric in the deformed OFETs, the gate leakage current (I_{GS}) together with I_{DS} were recorded in the transfer characteristics after multiple bending cycles at the radii of 100 and 500 μm. The results are presented in **Figure 10**. After bending at the radius of 500 μm, I_{GS} remains at the same level as before deformation confirming a notion that a tensile strain of 0.45% does not induce defects in the parylene dielectric layer. In the case of the tensile strain of 2.25% at the radius of 100 μm, I_{GS} increases only slightly and remains still at a low level independent of the number of bending cycles. A minor increase of I_{GS} at low voltages can be related to the elongation at yield of parylene (of around 2.5%), at which irreversible structural changes are induced into the material.[53] Nevertheless, the increase of I_{GS} is negligible in comparison to the few orders of magnitude higher values of I_{DS}. Therefore, this factor does not need to be considered as a potential reason for the change in OFET performance upon its deformation.

3. Conclusions

When subjected to multiple deformation, DPP-DTT based flexible OFETs show high fatigue resistance. Deformation of the DPP-DTT films at the radius of 500 μm, which corresponds to a tensile strain of 0.45%, reveal a stable transistor performance even after 100 bending cycles, independent of the film thickness. Cyclic bending at a smaller radius of 100 μm, i.e., beyond the elongation at yield of the parylene dielectric, induces drastic macroscopic fractures in the DPP-DTT films. Despite serious defects at the tensile strain of 2.25%, the OFETs still show a good reliability. This is mainly attributed to the robust parylene dielectric layer that prevents gate leakage during device operation and provides high fatigue resistance of the active DPP-DTT film. The main decrease of the device performance is observed mainly during the first bending cycles at which the fractures are probably formed. It is assumed that the cracks are formed through the entire thickness of the 30 nm thick film, thus creating trapping sites at the DPP-DTT/parylene interface at which the charge carrier transport takes place. The interface of the thicker DPP-DTT films is less affected by the deformation-induced defects, which results in a more stable device performance upon

Figure 10. Transfer characteristics with I_{DS} and I_{GS} of OFETs with 30 nm DPP-DTT film before and after 5 and 100 bending cycles at the radius of a) 500 μm and b) 100 μm.

**ADVANCED
SCIENCE NEWS**

www.advancedsciencenews.com

**ADVANCED
MATERIALS
INTERFACES**

www.advmatinterfaces.de

cyclic deformation. These insights are important for the design of future OFETs characterized by still higher fatigue resistance. This work has also revealed a unique potential of the experimental bending setup presented to systematically evaluate the device performance of flexible electronics during precise deformation. In the future, this potential will be further exploited in the characterization of other semiconducting materials applied in different semiconductor devices.

4. Experimental Section

Materials: DPP-DTT with M_w of 290 688 was purchased from Osilla Ltd. Solvent-dehydrated 1,2-dichlorobenzene was purchased from Sigma Aldrich, Parylene C precursor DPX-C was purchased from Specialty Coating Systems (SCS). All materials were used as received.

Atomic Force Microscopy: To investigate the surface topography of the DPP-DTT films before and after bending, 10.0 μm × 10.0 μm AFM images were recorded in tapping mode using Nanosurf C3000 Atomic Force Microscope with MikroMasch cantilevers (320 kHz resonance frequency, force constant 40 Nm^{-1}).

Optical Microscopy: An optical inspection of the films before and after mechanical deformation was performed with a Keyence VHX 70000 optical microscope. The 3D visualization was prepared by using Keyence software.

Transistor Fabrication: Flexible transistors, composed of 3.0 μm parylene substrate, 100 nm silver gate electrode, 1.5 μm parylene dielectric layer, either 30 or 120 nm DPP-DTT active film, and 100 nm of gold electrodes, were fabricated in a bottom-gate top-contact (BGTC) electrode configuration. The entire fabrication process was performed on a glass carrier substrate from which the devices were then peeled off in order to carry out deformation experiments. Parylene was deposited by chemical vapor deposition (CVD) using a SCS Labcoater PDS 2010. The gate electrode was deposited on the parylene through specially designed shadow masks (fabricated by laser ablation) in a high vacuum thermal deposition process at 1×10^{-5} mbar. The channel dimensions were 1 mm width and 250 μm length. The DPP-DTT solution was spin-coated at two sets of conditions to achieve two different magnitudes of film thickness. A 30 nm thick film was obtained from 5 mg mL^{-1} 1,2-dichlorobenzene (DCB) solution spin-coated at 2000 rpm with an acceleration of 1000 rpm s^{-1} for 60 s. The 120 nm thick film was deposited from 10 mg mL^{-1} DCB solution spin-coated at 1000 rpm with an acceleration of 100 rpm s^{-1} for 60 s. The films were then annealed under reduced pressure of 1×10^{-3} mbar for 6 h at 120 °C to remove residual solvent. During device fabrication any influence of thermal strains was reduced as far as possible. To complete the transistor BGTC configuration, the source and drain electrodes were thermally evaporated at the same conditions as the gate electrode was. The bottom-gate top-contact OFET architecture was applied to achieve maximum strain in the active polymer film during bending. A protective layer on top of the semiconductor was omitted in order to investigate the damage of the semiconductor layer.

Bending Experiments: The ready transistors were carefully peeled off from the glass support and installed in the especially designed setup for deformation experiments. The OFETs were placed on the bending knife with a defined curvature to achieve bending radii of 100 or 500 μm during convex deformation, as illustrated in Figure 1b. In the OFET architecture, the DPP-DTT film was located as the top layer to encounter the maximum strain at a defined bending radius. The OFET position on the bending knife was stabilized by the clamps assembled at the bending arm and equipped with electrodes to ensure an electrical connection to the source meter (Figure 1b). Using a microscope equipped with a digital camera, the bending knife was positioned precisely between source and drain electrodes in the transistor channel to expose only the active area of DPP-DTT under strain (Figure 1c). To deform the OFETs one arm was moved to 90° in one direction. The bending setup was connected to a Keithley 2634B source meter that allowed in situ electrical characterization after a defined number of bending cycles.

OFET Characterization: The OFET output characteristics were measured at drain–source voltages (V_{DS}) swept between 0 and −40 V, for a series of gate–source voltages (V_{GS}) varied from 0 to −50 V at a step of 10 V. The transfer characteristics were measured after applying a constant V_{DS} of −5 V for the linear and −50 V for the saturation regime at V_{GS} swept between 10 and −50 V. The bias stress measurement was performed by an application of constant V_{DS} of −50 V and constant V_{GS} of −40 V, over a time of 300 s. The electrical characterization was performed for 50 devices. All electrical measurements took place in ambient environment with a maximum duration of ≈6 h for each sample.

Supporting Information

Supporting Information is available from the Wiley Online Library or from the author.

Conflict of Interest

The authors declare no conflict of interest.

Author Contributions

P.K., T.M., W.P. designed and P.K. fabricated and characterized the OFET devices; W.W. investigated the films by AFM; P.K., A.A., and W.W. analyzed the data; M.G.L., A.N., A.A., and P.K. optimized and performed the parylene deposition; M.T. designed and fabricated the shadow masks; P.K., W.W., A.A., T.M., designed the bending setup. T.M. and W.P. supervised the project. P.K. and W.P. wrote the manuscript with contributions from all authors. All authors have given approval to the final version of the manuscript.

Data Availability Statement

The data that support the findings of this study are available from the corresponding author upon reasonable request.

[1] D. Rodriquez, *ACS Appl. Mater. Interfaces* **2017**, *9*, 8855.
[2] N. Lu, D. H. Kim, *Soft Robot.* **2014**, *1*, 53.
[3] A. C. Arias, J. D. MacKenzie, I. McCulloch, J. Rivnay, A. Salleo, *Chem. Rev.* **2010**, *110*, 3.

ADVANCED
SCIENCE NEWS
www.advancedsciencenews.com

ADVANCED
MATERIALS
INTERFACES
www.advmatinterfaces.de

[4] R. A. Nawrocki, *Adv. Funct. Mater.* **2019**, *29*, 1906908.

[5] H. Yan, *Nature* **2009**, *457*, 679.

[6] D. Tobjörk, R. Österbacka, *Adv. Mater.* **2011**, *23*, 1935.

[7] M. Barbaro, A. Caboni, P. Cosseddu, G. Mattana, A. Bonfiglio, *IEEE Trans. Inf. Technol. Biomed.* **2010**, *14*, 758.

[8] M. Kaltenbrunner, *Nature* **2013**, *499*, 458.

[9] T. Sekitani, U. Zschieschang, H. Klauk, T. Someya, *Nat. Mater.* **2010**, *9*, 1015.

[10] T. Yokotaa, *Proc. Natl. Acad. Sci. USA* **2015**, *112*, 14533.

[11] Y. Zang, F. Zhang, D. Huang, X. Gao, C. A. Di, D. Zhu, *Nat. Commun.* **2015**, *6*, 1.

[12] R. A. Nawrocki, N. Matsuhisa, T. Yokota, T. Someya, *Adv. Electron. Mater.* **2016**, *2*, 1500452.

[13] S. Fratini, M. Nikolka, A. Salleo, G. Schweicher, H. Sirringhaus, *Nat. Mater.* **2020**, *19*, 491.

[14] J. Choi, *Chem. Mater.* **2019**, *31*, 3163.

[15] Y. J. Lee, Y. U. Lee, H. W. Yeon, H. A. S. Shin, L. A. Evans, Y. C. Joo, *Appl. Phys. Lett.* **2013**, *103*, 241904.

[16] P. Cosseddu, G. Tiddia, S. Milita, A. Bonfiglio, *Org. Electron.* **2013**, *14*, 206.

[17] P. Cosseddu, S. Milita, A. Bonfiglio, *IEEE Electron Device Lett.* **2012**, *33*, 113.

[18] D. Choi, *Chem. Mater.* **2016**, *28*, 1196.

[19] S. Savagatrup, X. Zhao, E. Chan, J. Mei, D. J. Lipomi, *Macromol. Rapid Commun.* **2016**, *37*, 1623.

[20] H. J. Kim, *ACS Appl. Mater. Interfaces* **2017**, *9*, 14120.

[21] F. Sugiyama, *Macromolecules* **2018**, *51*, 5944.

[22] Y. C. Lin, F. H. Chen, Y. C. Chiang, C. C. Chueh, W. C. Chen, *ACS Appl. Mater. Interfaces* **2019**, *11*, 34158.

[23] H. C. Wu, *Macromolecules* **2016**, *49*, 8540.

[24] S. Savagatrup, *Energy Environ. Sci.* **2015**, *8*, 55.

[25] Y. W. Huang, *Chem. Mater.* **2020**, *32*, 7370.

[26] A. D. Printz, A. S. C. Chiang, S. Savagatrup, D. J. Lipomi, *Synth. Met.* **2016**, *217*, 144.

[27] M. A. Alkhadra, S. E. Root, K. M. Hilby, D. Rodriquez, F. Sugiyama, D. J. Lipomi, *Chem. Mater.* **2017**, *29*, 10139.

[28] T. Sekine, D. Kumaki, S. Tokito, *Materials* **2017**, *10*, 2.

[29] K. Fukuda, Y. Takeda, M. Mizukami, D. Kumaki, S. Tokito, *Sci. Rep.* **2014**, *4*, 4.

[30] H. Ren, N. Cui, Q. Tang, Y. Tong, X. Zhao, Y. Liu, *Small.* **2018**, *14*, 1.

[31] D. J. Lipomi, J. A. Lee, M. Vosgueritchian, B. C. K. Tee, J. A. Bolander, Z. Bao, *Chem. Mater.* **2012**, *24*, 373.

[32] F. A. Viola, *Nat. Commun.* **2021**, *12*, 2.

[33] H. Ren, Q. Tang, Y. Tong, Y. Liu, *Materials* **2017**, *10*, 1.

[34] M. Liu, H. Wang, Y. Tong, X. Zhao, Q. Tang, Y. Liu, *IEEE Electron Device Lett.* **2018**, *39*, 1183.

[35] H. T. Yi, M. M. Payne, J. E. Anthony, V. Podzorov, *Nat. Commun.* **2012**, *3*, 1257.

[36] K. Fukuda, T. Sekine, R. Shiwaku, T. Morimoto, D. Kumaki, S. Tokito, *Sci. Rep.* **2016**, *6*, 1.

[37] L. Zhang, *Adv. Mater.* **2013**, *25*, 5455.

[38] K. Taguchi, *Adv. Mater.* **2021**, *33*, 1.

[39] T. Marszalek, M. Gazicki-Lipman, J. Ulanski, *Beilstein J. Nanotechnol.* **2017**, *8*, 1532.

[40] D. Bhat, S. Jena, A. Babusenan, J. Bhattacharyya, D. Ray, *Synth. Met.* **2019**, *255*, 116108.

[41] J. Oh, *IEEE Trans. Device Mater. Reliab.* **2018**, *18*, 1.

[42] L. G. Kaake, P. F. Barbara, X. Y. Zhu, *J. Phys. Chem. Lett.* **2010**, *1*, 628.

[43] P. A. Bobbert, A. Sharma, S. G. J. Mathijssen, M. Kemerink, D. M. De Leeuw, *Adv. Mater.* **2012**, *24*, 1146.

[44] M. Kunii, H. Iino, J. Hanna, *Appl. Phys. Lett.* **2017**, *110*, 243301.

[45] S. Bisoyi, U. Zschieschang, M. J. Kang, K. Takimiya, H. Klauk, S. P. Tiwari, *Org. Electron.* **2014**, *15*, 3173.

[46] R. Ahmed, A. Kadashchuk, C. Simbrunner, G. Schwabegger, M. A. Baig, H. Sitter, *ACS Appl. Mater. Interfaces* **2014**, *6*, 15148.

[47] B. Blülle, R. Häusermann, B. Batlogg, *Phys. Rev. Appl.* **2014**, *1*, 1.

[48] M. Geiger, *Adv. Mater. Interfaces* **2020**, *7*, 1902145.

[49] W. L. Kalb, B. Batlogg, *Phys. Rev. B* **2010**, *81*, 1.

[50] W. Shi, Y. Zheng, J. Yu, A. D. Taylor, H. E. Katz, *Appl. Phys. Lett.* **2016**, *109*, 143301.

[51] M. Li, C. An, T. Marszalek, M. Baumgarten, K. Müllen, W. Pisula, *Adv. Mater.* **2016**, *28*, 2245.

[52] L. Janasz, *Langmuir* **2017**, *33*, 4189.

[53] R. P. Von Metzen, T. Stieglitz, *Biomed. Microdevices* **2013**, *15*, 727.